Fu et al. *Microsystems & Nanoengineering* (2026)12:5
https://doi.org/10.1038/s41378-025-01136-6

Microsystems & Nanoengineering
www.nature.com/micronano

ARTICLE Open Access

3D-printed barbed microneedle electrodes for biosensing and drug delivery in wound management

Xinyu Fu[1], Zhengnan Sun[1], Jun Gu[2], Ruiqi Liu[3], Meng Ma[4], Xuelei Ma[5], Yi-Ping Ho[6], Xiaosheng Zhang[1]✉ and Yi Zhang[1,7]✉

Abstract

Chronic wounds represent a major global healthcare burden, demanding integrated solutions for both continuous wound monitoring and on-demand therapeutic intervention. In this work, we present monolithic barbed microneedles (3D-BMN) for wound impedance sensing and barbed hollow microneedles (3D-BHMN) for drug delivery, fabricated with high-precision projection micro-stereolithography (PμSL) 3D printing. Inspired by natural barbed structures like bee stingers, the barbed geometry balances penetration efficiency with mechanical interlocking, enabling stable anchorage to wound dressings. Conductivization with Ag/AgCl and AuNPs imparts robust electrochemical performance, allowing accurate monitoring of wound impedance, which correlates with wound status. 3D-BHMN integrates an ultrasonic atomizer for efficient drug delivery. A closed-loop feedback system couples 3D-BMN and 3D-BHMN, forming a closed-loop system for on-demand delivery of therapeutic agents modulated by the sensed impedance value that aligns with the dynamic wound status. This integrated platform advances smart wound management by combining diagnostics and therapeutics, offering broad translational potential.

Introduction

Wound management represents a critical pillar of modern healthcare. Globally, over 60 million individuals suffer from chronic wounds. In China, diabetic foot ulcers alone account for tens of billions of Yuan in annual medical expenditures[1]. This huge burden continues to escalate, driven by an aging population and growing prevalence of diabetes, underscoring an urgent need for advanced wound management strategies.

Traditional wound dressings, such as hydrocolloids and foams, have long served as the standard of wound care. These dressing materials provide moderate protection against bacterial colonization and maintain a moist microenvironment conducive to wound healing. However, the passive nature of these dressings significantly limits their therapeutic functionalities. Lacking the capacity to directly monitor key biomarkers associated with wound healing progression, these dressings offer no real-time information on wound status. As a result, healthcare practitioners must frequently remove them for inspection[2–6], an intervention that risks secondary trauma, disrupts the delicate healing cascade, and ultimately delays wound recovery. Additionally, traditional dressings are incapable of on-demand drug delivery, limiting their applications for personalized responsive wound treatment.

Microneedles represent an emerging class of minimally invasive technology for painless transdermal biosensing and drug delivery[7–12]. Despite their potential, current microneedle-based systems are limited by insufficient mechanical anchorage. Conventional cone- or pyramid-shaped designs frequently dislodge from target tissues over extended durations, thereby significantly compromising their utility in applications requiring continuous

Correspondence: Xiaosheng Zhang (zhangxs@uestc.edu.cn) or Yi Zhang (yi_zhang@uestc.edu.cn)
[1]School of Integrated Circuit Science and Engineering, University of Electronic Science and Technology of China, Chengdu, China
[2]Department of Cardiovascular Surgery, West China Hospital, Sichuan University, Chengdu, China
Full list of author information is available at the end of the article
These authors contributed equally: Xinyu Fu, Zhengnan Sun.

monitoring. Among a diverse range of microneedle-based drug delivery platforms[13–16], hollow microneedles are well-suited for sustained on-demand drug administration; yet conventional fabrication approaches for such structures remain cumbersome, often involving multiple processing steps and extended fabrication cycles.

To tackle these challenges, we have developed two classes of 3D-printed barbed microneedles (3D-BMN): a sensing variant for real-time wound impedance monitoring, and a hollow variant (3D-BHMN) optimized for on-demand therapeutic drug delivery. Leveraging micro 3D printing technology, we achieved monolithic fabrication of both 3D-BMN and 3D-BHMN structures with high precision. The designs incorporate intricate bioinspired barbs inspired by the natural anchoring mechanisms of bee stingers[17], to enable robust mechanical interlocking with wound dressings, effectively preventing dislodgement and facilitating long-term stable deployment. The sensing 3D-BMN enables continuous real-time monitoring of wound impedance, which is strongly correlated with wound hydration, inflammatory burden, and bacterial load, thereby providing immediate and actionable feedback on healing trajectories[18,19]. In parallel, the hollow 3D-BHMN integrates a closed-loop control module based on impedance feedback, which triggers on-demand drug release, enabling condition-responsive and autonomous therapeutic interventions. This synergistic integration of real-time monitoring and precision therapeutics constitutes a significant advancement in chronic wound management. In general, our device distinguishes itself from prior works in two key aspects. First, it achieves system-level integration—combining 3D-BMN (sensing) and 3D-BHMN (drug delivery) into a closed-loop system with "sensing-triggered delivery," unlike studies focusing solely on fabrication (Ghosh et al., 2025)[20] or structure (Chen et al., 2018)[21]. Second, its one-step micro-3D printing creates hollow microneedles (150 μm channels) with barbs (50 μm) simultaneously. By addressing the challenges in long-term electrode stability, biosensing accuracy, and intelligent drug delivery, the barbed microneedle system demonstrated in this study holds profound potential for reshaping wound management practice and improving clinical outcomes.

Results

Fabrication of 3D-BMN and 3D-BHMN

Traditional microneedles frequently detach from biological tissues and dressing materials during prolonged wear, primarily attributed to skin tension, muscle movement, or bodily fluids. This instability can result in inaccurate sensing and inconsistent delivery of therapeutic agents, compromising treatment efficiency. Furthermore, the limited contact duration of single-use microneedles shows low therapeutic efficacy and necessitates repeated administrations, exacerbating tissue trauma and patient discomfort. To overcome these limitations, we engineered barbed microneedles by mimicking natural microstructures with anchorage, most notably, the honeybee stingers. Scanning electron microscopy (SEM) images of a honeybee stinger (Fig. 1a) reveal its distinct barbed morphology. In 3D-BMN, the 3D-printed barbs on the microneedles form robust mechanical interlocks with wound dressing materials, such as agarose (Fig. 1b). This structure significantly enhances microneedle retention by resisting external forces arising from skin contraction or limb movement, thereby extending the stable operation duration of the microneedles.

Schematic designs of both sensing 3D-BMN and delivery 3D-BHMN are illustrated in Fig. 1c. Each microneedle features a two-layer design with six barbs per layer angled at 45°, a configuration optimized to maximize mechanical anchorage and minimize trauma caused by insertion. Both 3D-BMN and 3D-BHMN were fabricated using projection micro stereolithography (PμSL), a variant of vat photopolymerization (VPP) 3D printing technology (Fig. 1d(i)). Given that the 3D-printed constructs are composed of non-conductive resin, a sequential surface modification protocol was developed to render 3D-BMN electrically conductive for electrochemical sensing (Fig. 1d(ii)). The first step involved spray-coating conductive Ag/AgCl paint onto the microneedle surfaces. This not only imparts conductivity but also introduces bioactive silver ions that act as non-toxic antioxidants and offer intrinsic antibacterial properties, thereby improving biocompatibility for long-term use. However, the electrochemical performance of the spray-coated Ag/AgCl layer alone was insufficient for high-sensitivity monitoring. To enhance functionality, a secondary layer of gold nanoparticles (AuNPs) was deposited via in situ redox reaction. Specifically, the Ag/AgCl-coated 3D-BMN was immersed in a solution containing sodium citrate ($Na_3C_6H_5O_7$) and chloroauric acid ($HAuCl_4$), enabling the deposition of AuNPs on the Ag/AgCl surface, which significantly enhanced the electrochemical performance of 3D-BMN electrodes[22].

Figure 1e(i) presents the physical appearance of the sensing-oriented 3D-BMN before and after conductivization. Post-conductivization, its surface exhibited a characteristic silver hue interspersed with localized purple spots. The hollow channels and barbed structures of 3D-BHMN were clearly evident in the optical images (Fig. 1e(ii)). Optical microscopy of 3D-BMN (Fig. 1f) revealed a well-defined structure with high-fidelity features and morphological consistency.

Mechanical characterization of 3D-BMN

Barbs are strategically incorporated into the microneedle design to anchor the microneedles securely within

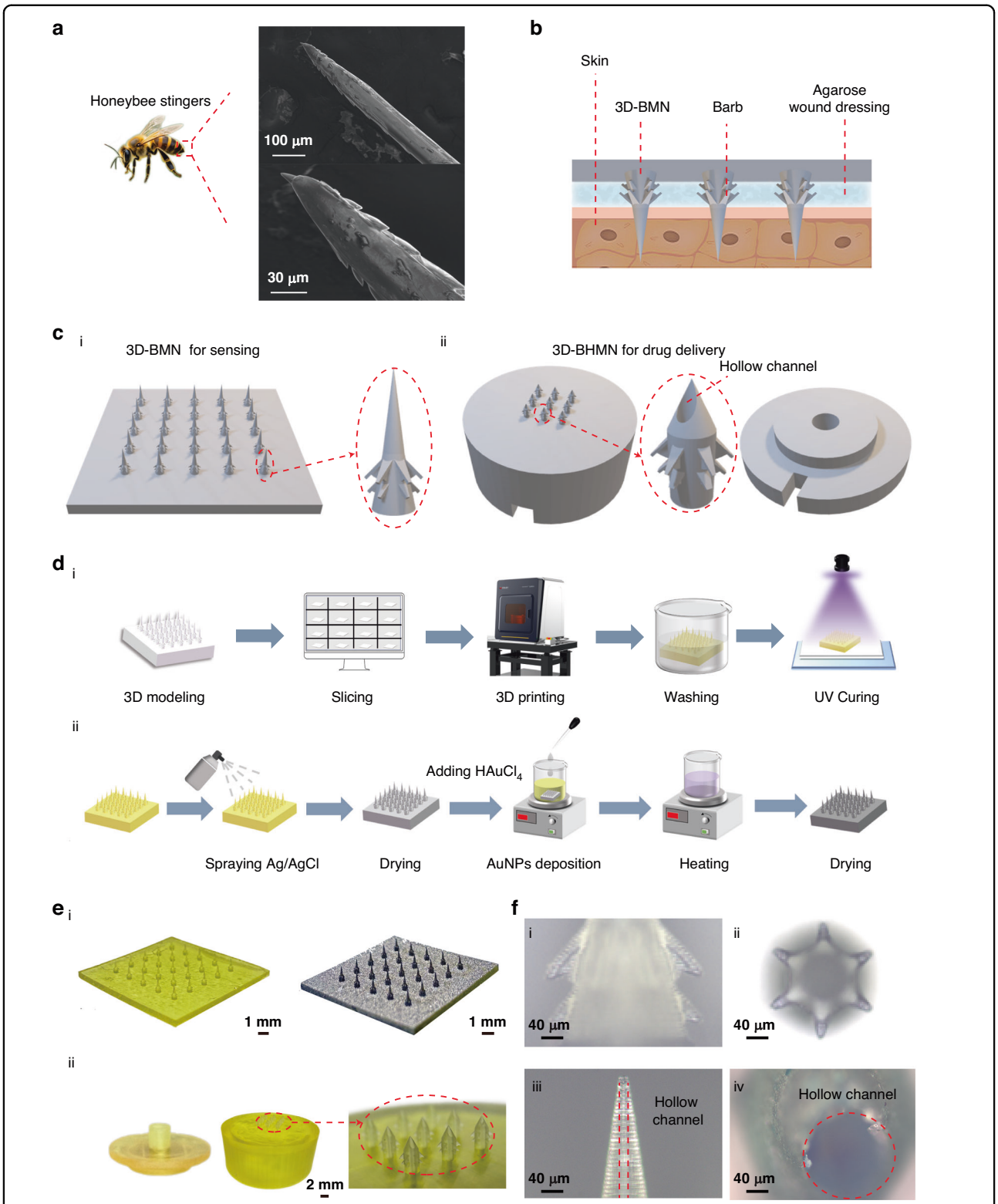

Fig. 1 Fabrication process and physical images of 3D-BMN and 3D-BHMN. a SEM images of a honeybee stinger, showing the distinct barbed morphology. **b** Schematic illustration of the operation principle of 3D-BMN. **c** i Design schematics of 3D-BMN for sensing. ii Design schematics of 3D-BHMN for drug delivery. **d** i Fabrication of the 3D-BMN resin matrix via PμSL technology. ii Conductivization process of 3D-BMN through Ag/AgCl spray coating and AuNP deposition. **e** i Optical images of 3D-BMN before and after conductivization. ii Optical images of 3D-BHMN. **f** Optical microscopy images of barbed microneedles, demonstrating their morphological characteristics

wound dressings to prevent detachment during prolonged wear, while maintaining smooth insertion through the dressing and into the skin tissue with minimal resistance. To systematically investigate how structural parameters of barbs, including barb angle, barb count, and layer count, influence the insertion and retraction forces of microneedles, a high-precision texture analyzer was used to simulate these dynamic mechanical interactions using an agarose-based wound dressing model (Fig. 2a). The agarose hydrogel is a common wound dressing model which provides a physiologically relevant test platform for real-world assessment of microneedle mechanics.

In the experimental setup, microneedles were rigidly mounted onto the texture analyzer probe, positioned vertically above the agarose model. The probe pressed against the wound dressing model at a constant velocity of 1 mm/s—mirroring clinically relevant insertion rates—until the microneedles were fully inserted into the hydrogel. Retraction was subsequently performed at the same rate to quantify withdrawal resistance. Each condition was tested in triplicate to account for stochastic variations, generating force–displacement curves from which quantitative mechanical performance metrics were derived.

A series of microneedle prototypes with systematically varied barb angles, barb numbers, and layer configurations was fabricated and tested (Fig. 2b–d). For experimental clarity and visualization, only a single microneedle was 3D-printed for observation. The primary objective was to identify an optimal barb configuration that balances the ease of insertion and anchorage strength by minimizing insertion resistance to reduce patient discomfort and tissue damage, while maximizing anchorage strength to prevent undesired detachment. The wound dressing model consisted of 5 wt% agarose hydrogel, which closely matched the hardness and elastic modulus of commercially available hydrocolloid dressings[23–27], thereby creating a physiologically relevant testing environment. Additionally, its transparency enabled direct real-time visual observation of barb–dressing interactions during insertion and retraction. These unique properties make agarose a gold standard for microneedle biomechanical testing.

Experimental results revealed several key mechanistic insights (Fig. 2b–d). First, both insertion and retraction forces showed a significant positive correlation with barb angle. As the barb angle increased, insertion resistance rose due to increased contact area, but the enhanced mechanical interlocking with agarose dressing improved anchorage strength. Notably, excessively large barb angle caused severe gel deformation during insertion, often leading to tip damage or dressing tearing. Based on these findings, a 45° barb angle emerged as the optimal design for subsequent studies, as this configuration offered a favorable compromise: insertion force remained sufficiently low to minimize patient discomfort while retraction force was sufficient to ensure stable anchorage over extended periods during wear.

In addition to the barb angle, increasing the number of barbs and layer count further enhanced attachment strength. This improvement was attributed to an increased number of anchoring points and expanded contact interface between barbs and agarose, which distributed mechanical loads more evenly and minimized localized shear failure. Consequently, a double-layered design with 6 barbs angled at 45° per layer was adopted as the standard configuration for subsequent experiments.

The structural optimization establishes a robust microneedle system for long-term continuous biosignal monitoring, where stable microneedle anchorage reduces sensor drift and eliminates the need for frequent reapplication, thereby mitigating patient burden and infection risk. Altogether, the optimized 3D-BMN demonstrates clinical relevance and mechanical reliability.

Electrochemical characterization of 3D-BMN

SEM was used for morphological analysis of 3D-BMN spray-coated with Ag/AgCl, followed by AuNPs deposition (Fig. 3a). SEM images of Ag/AgCl-sprayed microneedles (Fig. 3a(i)) revealed a conductive layer composed of microscale Ag/AgCl flakes forming a stacked and relatively non-uniform structure, an artifact due to the manual spraying process. This morphological non-uniformity likely compromises the electrical conductivity and reproducibility of the 3D-BMN electrode interface, potentially diminishing the overall electrochemical performance.

In contrast, subsequent AuNP deposition (Fig. 3a(ii)) produced a hierarchical coating comprising clusters of AuNPs distributed over the basal Ag/AgCl flake layer. These AuNPs clusters arise from the self-assembly behavior of AuNPs, which tend to aggregate to minimize surface energy during deposition. This hierarchical micro-nano coating not only increases the effective surface area for electrochemical interactions but also enhances electrical conductivity, leading to improved electrochemical performance.

The density and uniformity of AuNP coverage were further tuned by varying sodium citrate concentration during the deposition process. Higher citrate concentrations resulted in denser and more uniform coverage of AuNPs on the microneedle surface (Fig. 3a(iii)). Energy dispersive spectroscopy (EDS) elemental mapping corroborated these observations (Fig. 3b(i–iii)), with Au-specific signals increasing progressively as sodium citrate concentration increased from 0.7% to 1.5%. These results highlight the critical role of sodium citrate in tuning AuNP loading and distribution on 3D-BMN, thereby

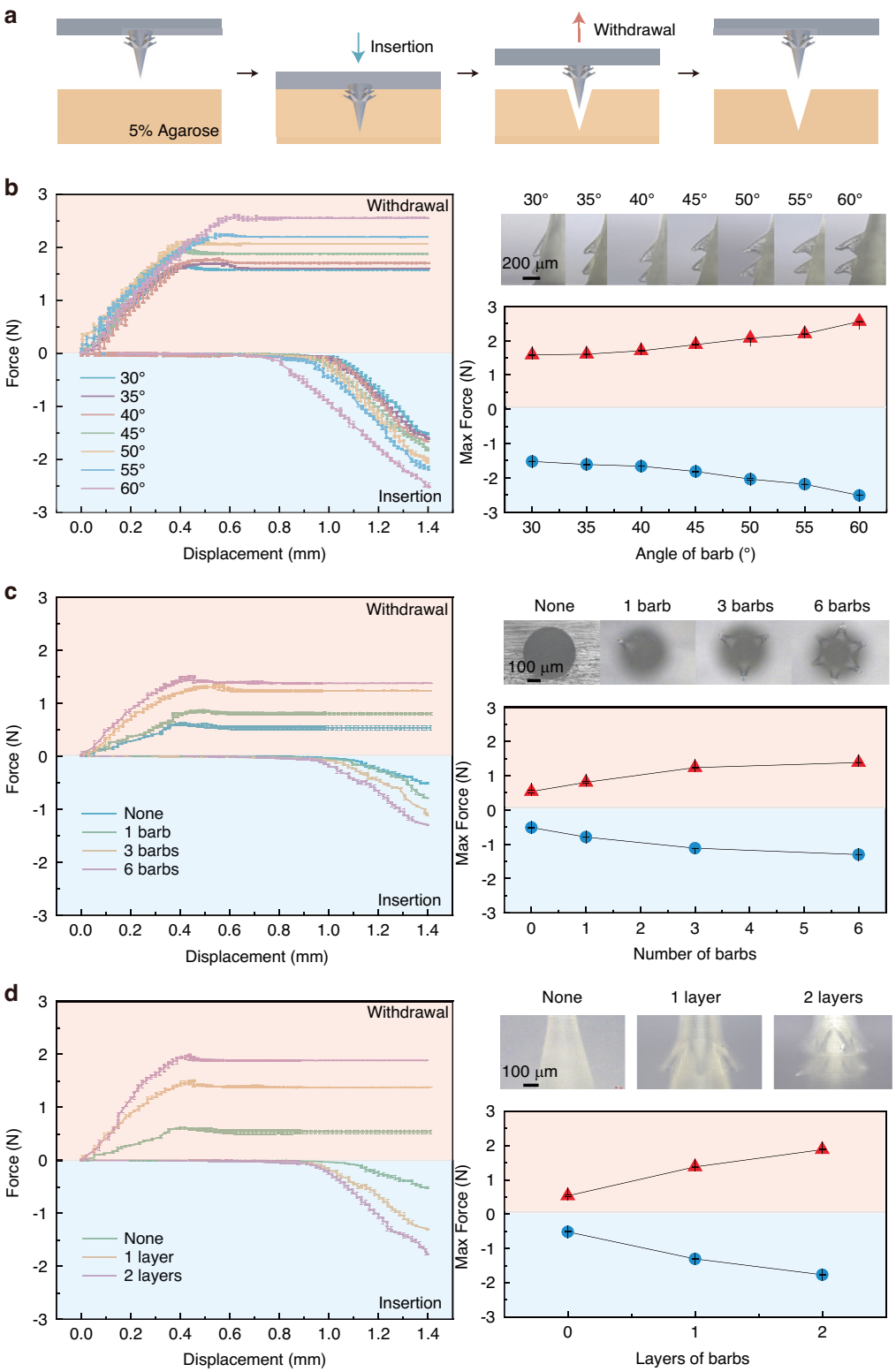

Fig. 2 Mechanical characterization of 3D-BMN. a Schematic of the setup for mechanical testing. **b** Stress–displacement curves for microneedles with different barb angles. **c** Stress–displacement curves for microneedles with different barb counts. **d** Stress–displacement curves for microneedles with different barb layer numbers

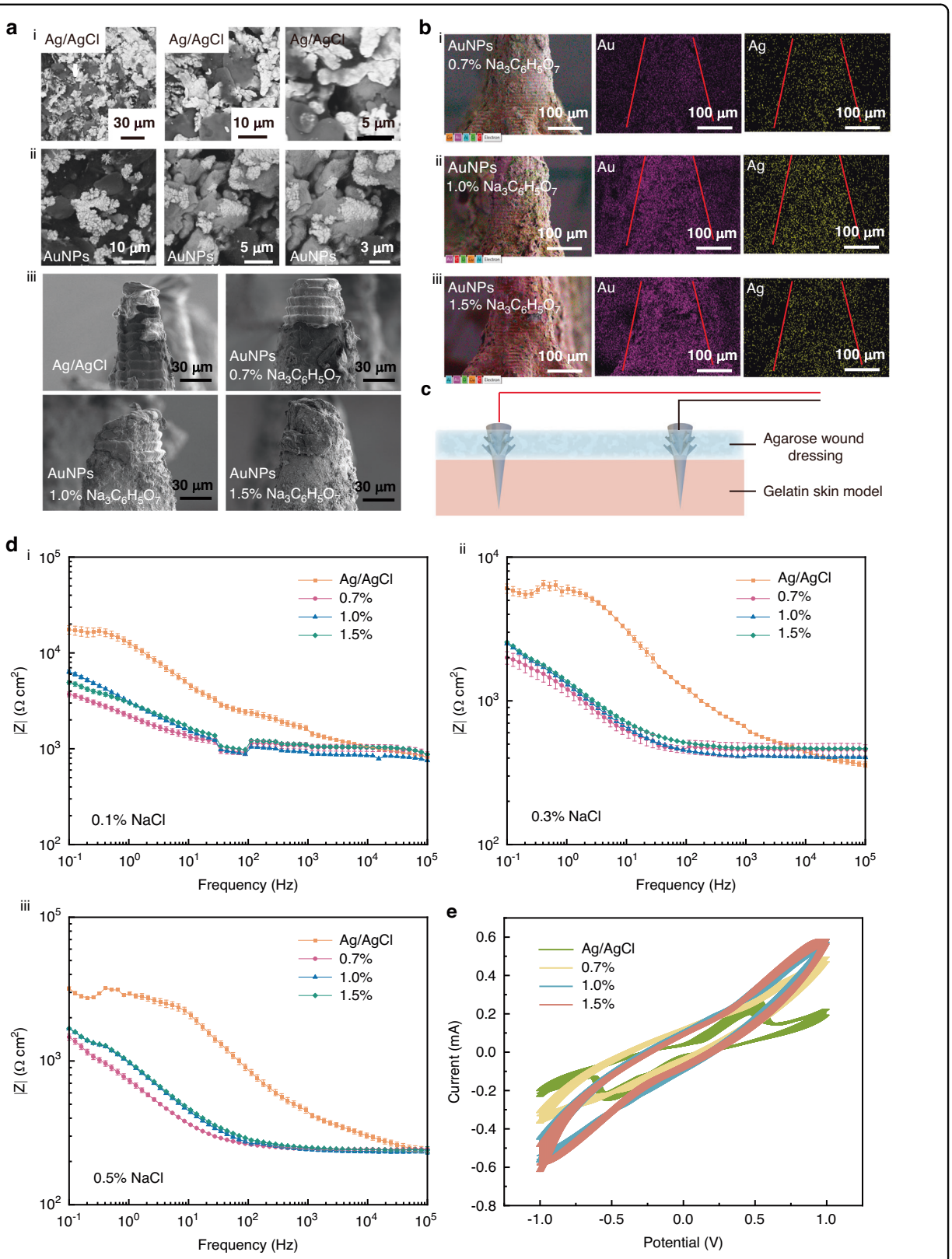

Fig. 3 (See legend on next page.)

(see figure on previous page)
Fig. 3 Electrochemical and structural characterization of the 3D-BMN. a SEM images of spray-coated Ag/AgCl microneedles and AuNPs-deposited microneedles. i Spray-coated Ag/AgCl microneedles. ii AuNPs-deposited microneedles. iii Spray-coated Ag/AgCl microneedles vs. Comparison of AuNPs-deposited microneedles under different sodium citrate concentrations. **b** EDS elemental mapping of spray-coated Ag/AgCl microneedles and AuNPs-deposited microneedles under varying sodium citrate concentrations. i Spray-coated Ag/AgCl microneedles. ii AuNPs-deposited microneedles in 0.7% sodium citrate solution. iii. AuNPs-deposited microneedles in 1.0% sodium citrate solution. iv AuNPs-deposited microneedles in 1.5% sodium citrate solution. The red line indicates the edge of the microneedles. **c** Schematic diagram of 3D-BMN testing for EIS and CV. **d** Comparative EIS curves of four microneedle types under different NaCl concentrations. i 0.1% NaCl concentration. ii 0.3% NaCl concentration. iii 0.5% NaCl concentration. **e** Comparative CV curves of four microneedle types

influencing the surface morphology and electrochemical performance.

To evaluate electrochemical performance under physiologically relevant conditions, measurements were conducted using an artificial skin model covered with agarose-based wound dressing. The artificial skin was composed of 5 wt% gelatin hydrogel to replicate the mechanical properties of human skin[28–32]. To simulate varying wound conditions, the skin model incorporated varying NaCl concentrations (0.1%, 0.3%, 0.5% w/w) to simulate progressive stages of wound inflammation with distinct impedance[18,19].

Electrochemical impedance spectroscopy (EIS) (Fig. 3d) measurements showed that 3D-BMN coated with AuNPs exhibited superior performance compared to bare Ag/AgCl electrodes, evidenced by substantially lower impedance and smoother impedance vs. frequency curves; these enhancements were accompanied by reduced standard deviations, indicating improved reproducibility. This enhanced performance is attributed to the hierarchical Ag/Au nanostructured interface, which facilitates efficient charge transfer and minimizes interfacial impedance. Cyclic voltammetry (CV) was further performed to characterize 3D-BMN. As AuNP coverage on the microneedle surface increased due to increasing sodium citrate concentration, peak currents increased progressively at given potentials (Fig. 3d). However, this trend plateaued for the 1.0% and 1.5% citrate groups, suggesting saturation of the microneedle surface with AuNPs. Collectively, these findings highlight the importance of AuNP coating for 3D-BMN in achieving reliable and reproducible electrochemical performance, contributing to high-performance microneedle-based biosensors under clinically relevant conditions.

Fabrication and characterization of 3D-BHMN-based drug delivery module

The reliable electrochemical performance of 3D-BMN enables real-time monitoring of impedance at the wound site, enabling us to develop an on-demand drug delivery system with integrated closed-loop feedback to achieve “sensing-triggered delivery”. The drug delivery module in the system is based on the 3D-BHMN, which is engineered by integrating an ultrasonic atomizer into 3D-BHMN (Fig. 4a). The device features an outer diameter of 24 mm, an inner diameter of 20 mm, and an overall height of 10 mm. A 3 mm-deep groove is designed on the top surface to house the power leads connecting the ultrasonic atomizer. The central hollow chamber incorporates a 2 mm-long microchannel array, each with a 0.4 mm diameter, whose centers are directly aligned with the centers of the 3D-BHMN hollow lumens (lumen diameter: 0.3 mm). A detachable top lid enables on-demand replenishment of therapeutic agents without requiring system disassembly, ensuring uninterrupted drug administration. The 3D-BHMN with an integrated drug chamber and the removable lid were fabricated separately via high-resolution 3D printing.

The drug delivery system is powered by a USB-interfaced driver board that provides regulated voltages to the ultrasonic atomizer, whose on–off states are governed via pulse-width modulation (PWM). In this configuration, the PWM signals excite an LC resonant circuit tuned to the resonant frequency of the ultrasonic atomizer. Upon activation, the ultrasonic atomizer oscillates at a high frequency, nebulizing the liquid drug within the chamber into aerosol droplets that are then channeled through the 3D-BHMN toward the target site. This mechanism ensures efficient, localized, and precise delivery of therapeutic agents via the 3D-BHMN with minimal invasion.

To evaluate the efficacy of ultrasound-assisted drug delivery via 3D-BHMN, a Franz diffusion cell system, a well-established in vitro model for evaluating transdermal drug delivery, was employed. The Franz diffusion cell comprises a donor compartment holding the drug formulation (in this case, drug-loaded 3D-BHMN) and a receptor compartment simulating underlying tissue to collect permeated drugs. The two compartments are separated by a semipermeable membrane mimicking the skin. In this study, the 5 wt% gelatin hydrogel skin model was used as the semipermeable membrane.

Three experimental groups were designed: (1) conventional topical delivery using a medical needle-punctured skin model as a baseline; (2) passive 3D-BHMN without ultrasound-induced aerosol delivery; (3) ultrasound-enhanced aerosol delivery via 3D-BHMN. A 0.1 wt% trypan blue solution served as the model drug for easy

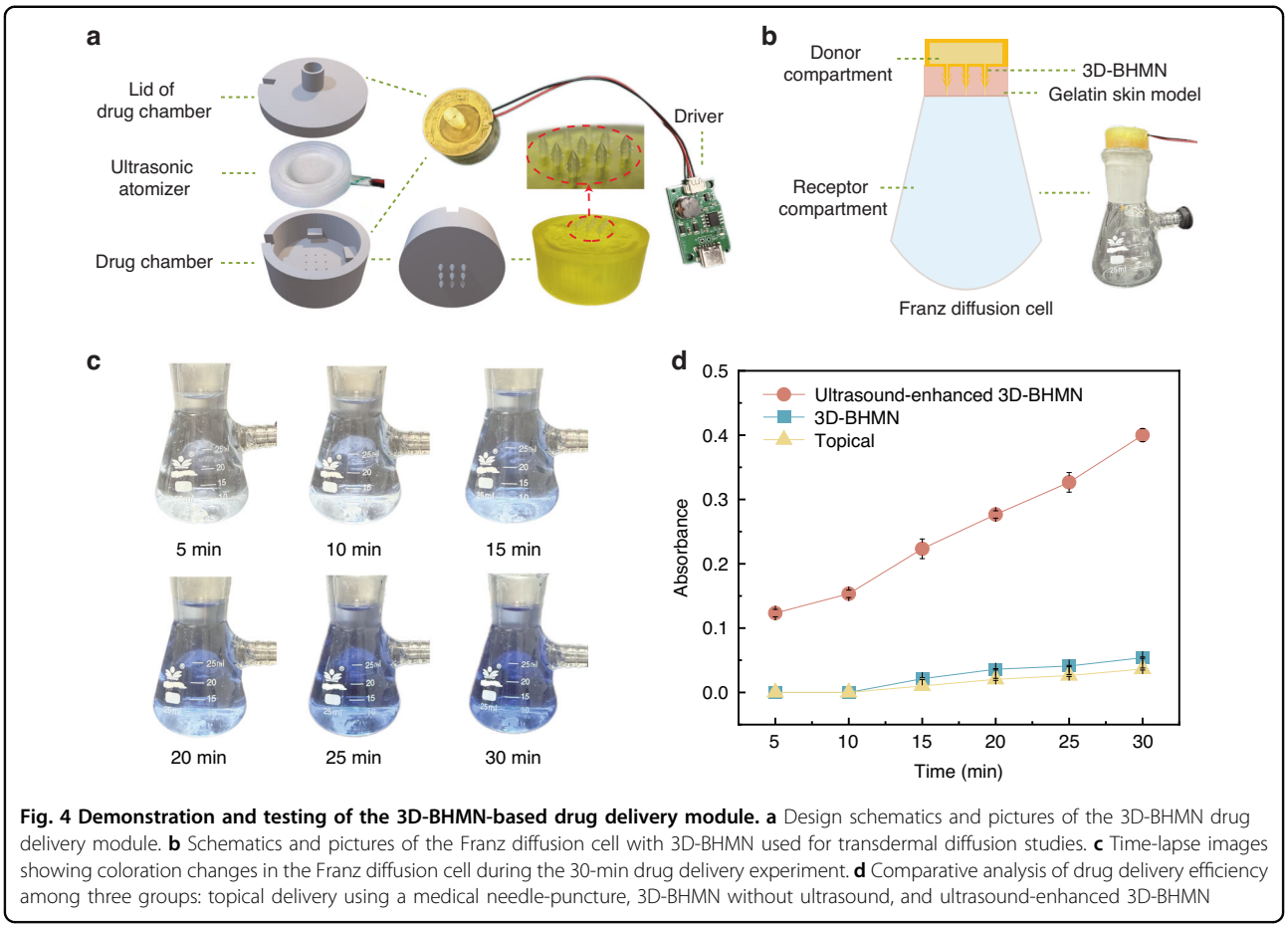

Fig. 4 Demonstration and testing of the 3D-BHMN-based drug delivery module. a Design schematics and pictures of the 3D-BHMN drug delivery module. **b** Schematics and pictures of the Franz diffusion cell with 3D-BHMN used for transdermal diffusion studies. **c** Time-lapse images showing coloration changes in the Franz diffusion cell during the 30-min drug delivery experiment. **d** Comparative analysis of drug delivery efficiency among three groups: topical delivery using a medical needle-puncture, 3D-BHMN without ultrasound, and ultrasound-enhanced 3D-BHMN

visualization, and the delivery process was maintained for 30 min in the Franz diffusion cell. Visual observation revealed progressive color changes in the receptor chamber over time (Fig. 4c), indicating increased drug accumulation. Quantitative analysis of drug delivery was conducted by measuring absorbance at 320 nm in samples extracted from the receptor compartment. The ultrasound-induced drug delivery via 3D-BHMN demonstrated significantly higher drug flux compared to the other two groups (Fig. 4d). These findings highlight the synergistic effect of integrating hollow microneedles and ultrasound-facilitated aerosolization in enhancing transdermal drug delivery. The hollow microchannels in the microneedles breach the stratum corneum, creating direct pathways for drug access to subcutaneous regions of the wound site, while ultrasonic atomization facilitates rapid distribution of drugs into these regions.

On-demand drug delivery with impedance feedback via 3D-BMN and 3D-BHMN

Impedance measurements serve as a sensitive biophysical indicator for monitoring wound healing progression, with characteristic impedance profiles correlating with distinct stages of tissue repair. A decline in impedance typically signals delayed healing, persistent inflammation, or infection—conditions resulting from impaired tissue remodeling and sustained high-moisture environments[18,19], which necessitate pharmacological interventions.

In this study, we present an integrated 3D-BMN biosensing and 3D-BHMN drug delivery platform that enables on-demand drug delivery via impedance feedback-controlled autonomous actuation (Fig. 5a). Central to this system is the STC89C52 microcontroller, which acts as the primary control module, orchestrating signal acquisition, processing, and actuation of the drug delivery module. Concurrently, an NE555 timer chip continuously monitors capacitor charge–discharge cycles directly correlated with impedance variations at the wound site. Following signal acquisition, raw data undergo amplification, noise reduction, and calibration to ensure the accuracy and reliability of impedance measurements. When the measured impedance falls below a user-defined threshold, which indicates potential wound deterioration due to infection or inflammation, the microcontroller triggers a relay to activate the ultrasonic

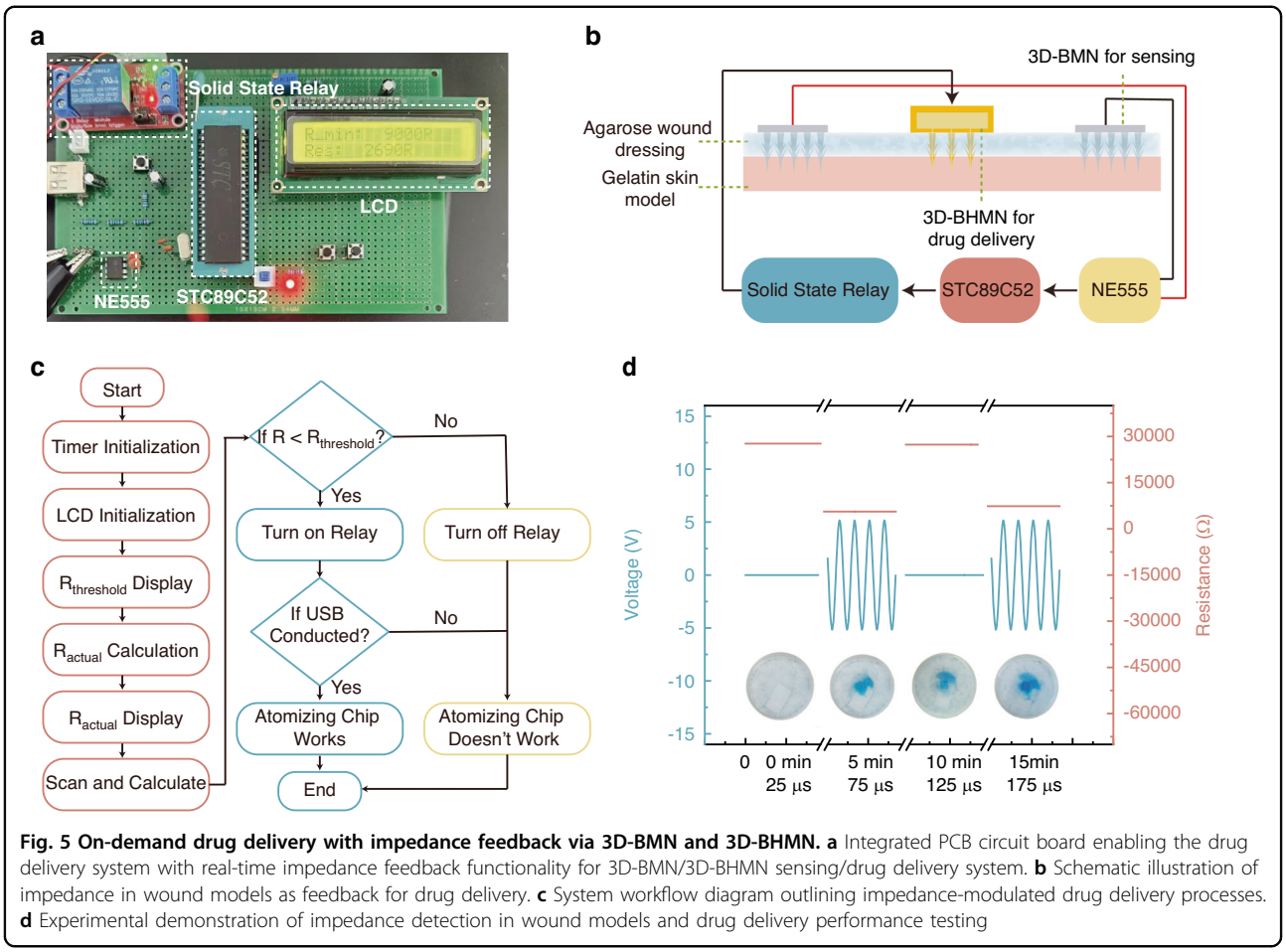

Fig. 5 On-demand drug delivery with impedance feedback via 3D-BMN and 3D-BHMN. a Integrated PCB circuit board enabling the drug delivery system with real-time impedance feedback functionality for 3D-BMN/3D-BHMN sensing/drug delivery system. **b** Schematic illustration of impedance in wound models as feedback for drug delivery. **c** System workflow diagram outlining impedance-modulated drug delivery processes. **d** Experimental demonstration of impedance detection in wound models and drug delivery performance testing

atomizer to deliver therapeutic agents to the wound site via the 3D-BHMN-based drug delivery module. This feedback-driven activation mechanism ensures responsive therapeutic dosing, minimizing unnecessary dosages and optimizing treatment efficacy.

System parameters, such as measured impedance and operational status, are displayed on an LCD1602 module. The threshold is adjustable via a user I/O interface, allowing dynamic adaptation to varying wound conditions and clinical scenarios.

The accuracy of impedance measurement was rigorously validated through a series of calibrations against precision resistors, demonstrating a maximum measurement error of 0.22%. These small deviations confirm the reliability of this system for impedance sensing in clinical applications. The integrated design, combining autonomous impedance sensing with on-demand drug delivery, holds significant promise for adaptive wound management. By continuously monitoring wound impedance and automatically triggering drug delivery when required, the system facilitates personalized and timely treatment, potentially improving healing outcomes and reducing the risk of complications.

To simulate practical and clinically relevant wound scenarios, in vitro experiments were performed with a gelatin wound model composed of 5% gelatin containing varying concentrations of NaCl covered by an agarose wound dressing (Fig. 5b). During operation, the 3D-BMN was fully inserted into the gelatin wound model, and the needle tip was ensured to penetrate the agarose wound dressing and reach a depth of ~600 μm into the wound model, a depth that is consistent with the standardized insertion depth validated in preliminary experiments to ensure stable contact with the target sensing region. Before recording the impedance data, a stabilization period of ~30 s was maintained, a duration optimized through preliminary pre-experiments to thereby avoid signal drift that caused errors in subsequent data analysis. The 3D-BMN sensor enables reliable electrical contact and signal transduction, ensuring accurate impedance monitoring. Powered by an external source, the integrated system continuously monitored impedance changes in the wound model. As shown in the flowchart (Fig. 5c), upon reaching the preset threshold, the drug delivery module is automatically activated. The results demonstrated that the system was able to accurately detect impedance variations

and deliver drugs on demand in a timely manner, underscoring its effectiveness in practical applications (Fig. 5d). When the impedance of the gelatin skin model fell below the threshold value, the driver board generated high-frequency oscillations to activate the ultrasonic atomizer, releasing the trypan blue solution through 3D-BHMN. Conversely, when impedance values remained above the threshold, oscillations were not triggered. As a result, the ultrasonic atomizer remained inactive, disabling drug delivery.

Discussion

This work presents a multifunctional platform integrating 3D-BMN biosensing and 3D-BHMN drug delivery modules for combined real-time wound impedance sensing with ultrasound-enhanced drug delivery in chronic wound management. Fabricated via PμSL, the optimized 45° barbed structure balances the ease of insertion and robust mechanical anchorage. Surface modifications via Ag/AgCl spraying and AuNPs deposition enhance electrical stability for precise and reliable impedance monitoring. The incorporation of ultrasonic atomization generates submicron aerosolized drug droplets, increasing transdermal penetration efficiency by multiple folds compared to passive delivery systems in gelatin skin models. Crucially, the impedance-based closed-loop feedback enables on-demand drug delivery, aligning drug administration with the wound healing progression. This monolithic platform integrates mechanical interlocking, sensing, and drug delivery at micron structural precision using high-precision 3D printing, demonstrating both technical sophistication and scalability. Collectively, this study establishes a foundation for next-generation smart wound dressings that integrate diagnostic monitoring with on-demand therapeutic administration. The proposed platform holds significant promise for improving clinical outcomes by responsive precision wound care, thereby reducing patients' burden and minimizing complications associated with chronic wounds.

Materials and methods

Materials

High-temperature resistant (HTL) resin was purchased from Boston Micro Fabrication Co., Ltd. The conductive silver spray paints were sourced from Shenzhen Jingzhe Technology Co., Ltd., and the chloroauric acid ($HAuCl_4$) solution and sodium citrate ($Na_3C_6H_5O_7$) were obtained from Jiangsu Aikon Biopharmaceutical R&D Co., Ltd. Gelatin, agarose, and sodium chloride were purchased from Chengdu Keweizhuo Technology Co., Ltd.

Preparation of 3D-BMN

3D-BMN was first modeled using SOLIDWORKS. Projection micro-stereolithography (PμSL) 3D printing (microArch® S240, BMF, China) was employed to fabricate 3D-BMNs from HTL photopolymer resin, followed by surface modification involving Ag/AgCl spray coating and nanogold deposition via a redox reaction, using 0.7%, 1.0%, and 1.5% $Na_3C_6H_5O_7$ in $HAuCl_4$ solution. The 3D-BMN has the following key dimensions: the base diameter of each microneedle is 400 μm, the total length (from the base to the tip) is 1300 μm, and the length of each barbed structure (measured from the edge of the microneedle shaft to the outermost end of the barb) is 350 μm. To ensure stable electrochemical sensing, the Ag/AgCl coating on 3D-BMN was prepared via a standardized spray process. Each 3D-BMN was fixed on a glass slide with non-conductive adhesive, with the microneedle shaft exposed. The microneedle was sprayed with Ag/AgCl conductive paint from both the front and back sides under the following conditions: spray distance = 25 cm, nozzle angle = 45° (relative to the microneedle axis), spray duration = 2 s per side. Following the spraying process, the device was dried in a 40 °C vacuum oven for 10 min to remove residual solvent and enhance coating adhesion. The specific experimental procedures for depositing gold nanoparticles are as follows: (1) Prepare a 0.01% aqueous solution of $HAuCl_4$ and 0.7%, 1.0%, and 1.5% aqueous solutions of $Na_3C_6H_5O_7$ using deionized water. (2) Take 100 mL of $HAuCl_4$ aqueous solution, heat it to boiling on a magnetic heating stirrer, attach a lead wire to the bottom of the microneedle, suspend the microneedle on the wall of the beaker, and add a certain amount of 0.7%, 1.0%, and 1.5% sodium citrate aqueous solutions, respectively, for three different types of 3D-BMNs after the microneedle is immersed. (3) Continue heating to maintain boiling; it will be observed that the pale yellow chloroauric acid aqueous solution quickly turns gray after the addition of sodium citrate, then changes to black, and subsequently stabilizes to a reddish-purple color. (4) After cooling to room temperature, remove the microneedle from the beaker and allow it to air-dry in a well-ventilated area.

Preparation of 3D-BHMN

3D-BHMN was first modeled using SOLIDWORKS. PμSL 3D printing technology was employed to directly fabricate 3D-BHMNs using HTL photopolymer resin as the raw material.

Based on the 3D-BHMN, the drug delivery module in the system is designed with an ultrasonic atomizer integrated into the 3D-BHMN structure. The ultrasonic atomizer operates with the following parameters: its operating voltage is 5 V, the corresponding operating current is 300 mA, and the resonant frequency (a core parameter for ensuring atomization efficiency) is set to ~110 kHz. This specific combination is optimized through

pre-testing to balance atomization performance, energy consumption, and long-term stability of the atomizer.

Construction of the real-time feedback impedance-modulated drug delivery system

The overall system's main control module is built around an STC89C52 microcontroller, with an NE555 chip deployed for real-time monitoring of capacitor charge–discharge cycles. Following signal processing and error correction, these cycles are converted into high-precision impedance values. The system triggers relay activation when the impedance falls below a preset minimum threshold, activating the atomization sheet. Medication is then dispersed onto the wound site through hollow microneedles via a nebulization mechanism. Detection results are visualized using an LCD1602 liquid crystal display and an infrared indicator on the relay, while the minimum impedance threshold can be adjusted in real-time via a key circuit module. This integrated design enables precise impedance-based sensing with user-configurable response parameters, integrating microcontroller logic with analog signal processing to achieve automated drug delivery.

Characterization and measurement

Mechanical properties were tested using a texture analyzer (Universal TA, Shanghai Tengba Instrument Technology Co., China) to evaluate insertion and extraction forces in agarose hydrogel, while electrochemical performance was assessed via cyclic voltammetry (CV) and electrochemical impedance spectroscopy (EIS) by a electrochemical workstation (CS300M, Wuhan Corrtest Instruments Corp., China) in gelatin models with varying NaCl concentrations. SEM and EDS images were acquired using a transmission electron microscope (Talos F200X, Thermo Fisher, USA). For system integration, an STC89C52 microcontroller-based circuit with NE555 resistance detection and LCD1602 display was developed to trigger an ultrasonic atomizer via relay control. Drug delivery efficiency was validated in Franz diffusion cells, comparing ultrasonic-enhanced 3D-BHMN delivery with traditional methods. All electrochemical experiments, including CV, EIS, and wound impedance monitoring, were conducted under a controlled laboratory environment temperature of 25 ± 1 °C.

Acknowledgements

Authors would like to thank the funding support by the National Key Research and Development Program of China (Xiaosheng Zhang: No. 2022YFB3206100), the National Natural Science Foundation of China (Yi Zhang: No. 62271107), the Natural Science Foundation of Sichuan Province (Yi Zhang: No. 2025ZNSFSC0464), the Key R&D Program of Mianyang (Xiaosheng Zhang: No. 2023ZYDF019), the Fundamental Research Funds for the Central Universities (Yi Zhang: No. ZYGX2022YGRH007).

Author details

[1]School of Integrated Circuit Science and Engineering, University of Electronic Science and Technology of China, Chengdu, China. [2]Department of Cardiovascular Surgery, West China Hospital, Sichuan University, Chengdu, China. [3]Department of Plastic and Burn Surgery, West China Hospital, Sichuan University, Chengdu, China. [4]School of Medicine, University of Electronic Science and Technology of China, Chengdu, China. [5]Department of Biotherapy, Cancer Center and State Key Laboratory of Biotherapy, West China Hospital, Sichuan University, Chengdu, China. [6]Department of Biomedical Engineering, The Chinese University of Hong Kong, HongKong, China. [7]Tianfu Jiangxi Laboratory, Chengdu, China

Data availability

The data that support the plots within this paper and other findings of this study are presented in the main article. Additional data related to this paper may be requested from the corresponding authors upon reasonable request.

Competing interests

The authors declare no competing interests.

Received: 27 August 2025 Revised: 31 October 2025 Accepted: 27 November 2025
Published online: 01 January 2026

References

1. Xiang, Z., Wang, H. & Li, H. Comorbidity risk and distribution characteristics of chronic diseases in the elderly population in China. *BMC Public Health* **24**, 360 (2024).
2. Ahmad, N. In vitro and in vivo characterization methods for evaluation of modern wound dressings. *Pharmaceutics* **15**, 42 (2023).
3. Dabiri, G., Damstetter, E. & Phillips, T. Choosing a wound dressing based on common wound characteristics. *Adv. Wound Care* **5**, 32–41 (2016).
4. Shi, C. et al. Selection of appropriate wound dressing for various wounds. *Front. Bioeng. Biotechnol.* **8**, 2020 (2020).
5. Weller, C. D., Team, V. & Sussman, G. First-line interactive wound dressing update: a comprehensive review of the evidence. *Front. Pharmacol.* **11**, 2020 (2020).
6. Zhou, L. et al. Rational design of intelligent and multifunctional dressing to promote acute/chronic wound healing. *ACS Appl. Bio Mater.* **5**, 4055–4085 (2022).
7. Henry, S., McAllister, D. V., Allen, M. G. & Prausnitz, M. R. Microfabricated microneedles: a novel approach to transdermal drug delivery. *J. Pharm. Sci.* **87**, 922–925 (1998).
8. DeMuth, P. C., Garcia-Beltran, W. F., Ai-Ling, M. L., Hammond, P. T. & Irvine, D. J. Composite dissolving microneedles for coordinated control of antigen and adjuvant delivery kinetics in transcutaneous vaccination. *Adv. Funct. Mater.* **23**, 161–172 (2013).
9. Luzuriaga, M. A., Berry, D. R., Reagan, J. C., Smaldone, R. A. & Gassensmith, J. J. Biodegradable 3D printed polymer microneedles for transdermal drug delivery. *Lab Chip* **18**, 1223–1230 (2018).
10. Kim, Y.-C., Park, J.-H. & Prausnitz, M. R. Microneedles for drug and vaccine delivery. *Adv. Drug Deliv. Rev.* **64**, 1547–1568 (2012).
11. Waghule, T. et al. Microneedles: a smart approach and increasing potential for transdermal drug delivery system. *Biomed. Pharmacother.* **109**, 1249–1258 (2019).
12. Donnelly, R. F., Raj Singh, T. R. & Woolfson, A. D. Microneedle-based drug delivery systems: microfabrication, drug delivery, and safety. *Drug Deliv.* **17**, 187–207 (2010).
13. Fu, X. et al. Unique benefits and challenges of 3D-printed microneedles. *IJB* **10**, https://doi.org/10.36922/ijb.1896 (2024).
14. Detamornrat, U., McAlister, E., Hutton, A. R. J., Larrañeta, E. & Donnelly, R. F. The role of 3D printing technology in microengineering of microneedles. *Small* **18**, 2106392 (2022).
15. Fukushima, K. et al. Two-layered dissolving microneedles for percutaneous delivery of peptide/protein drugs in rats. *Pharm. Res.* **28**, 7–21 (2011).
16. Eş, I., Kafadenk, A., Gormus, M. B. & Inci, F. Xenon difluoride dry etching for the microfabrication of solid microneedles as a potential strategy in transdermal drug delivery. *Small* **19**, 2206510 (2023).

17. Das, R. et al. Biomechanical evaluation of wasp and honeybee stingers. *Sci. Rep.* **8**, 14945 (2018).
18. Jiang, Y. et al. Wireless, closed-loop, smart bandage with integrated sensors and stimulators for advanced wound care and accelerated healing. *Nat. Biotechnol.* **41**, 652–662 (2023).
19. Kekonen, A. et al. Bioimpedance sensor array for long-term monitoring of wound healing from beneath the primary dressings and controlled formation of H_2O_2 using low-intensity direct current. *Sensors* **19**, 2505 (2019).
20. Ghosh, A. et al. Innovations in additive manufacturing approaches for the fabrication of advanced drug delivery platforms, biomimetics, and predictive 3D microphysiological interfaces. *J. Mater. Chem. B* **13**, 11928–11970 (2025).
21. Chen, Z. et al. Additive manufacturing of honeybee-inspired microneedle for easy skin insertion and difficult removal. *ACS Appl. Mater. Interfaces* **10**, https://doi.org/10.1021/acsami.8b09563 (2018).
22. Tyagi, H., Kushwaha, A., Kumar, A. & Aslam, M. A facile pH controlled citrate-based reduction method for gold nanoparticle synthesis at room temperature. *Nanoscale Res. Lett.* **11**, 362 (2016).
23. Gomer, R. H. et al. A serum amyloid P-binding hydrogel speeds healing of partial thickness wounds in pigs. *Wound Repair Regen.* **17**, 397–404 (2009).
24. Huang, W.-C. et al. A macroporous hydrogel dressing with enhanced antibacterial and anti-inflammatory capabilities for accelerated wound healing. *Adv. Funct. Mater.* **30**, 2000644 (2020).
25. Liu, X. et al. A tough, antibacterial and antioxidant hydrogel dressing accelerates wound healing and suppresses hypertrophic scar formation in infected wounds. *Bioactive Mater.* **34**, 269–281 (2024).
26. Su, T. et al. Mussel-inspired agarose hydrogel scaffolds for skin tissue engineering. *Bioactive Mater.* **6**, 579–588 (2021).
27. Su, W. et al. Chitosan/agarose hydrogel dressing: pH response real-time monitoring and chemo-/photodynamic therapy synergistic treatment of infected wounds. *Int. J. Biol. Macromol.* **277**, 134513 (2024).
28. Baït, N., Grassl, B., Derail, C. & Benaboura, A. Hydrogel nanocomposites as pressure-sensitive adhesives for skin-contact applications. *Soft Matter* **7**, 2025–2032 (2011).
29. Bir, C. A., Resslar, M. & Stewart, S. Skin penetration surrogate for the evaluation of less lethal kinetic energy munitions. *Forensic Sci. Int.* **220**, 126–129 (2012).
30. Choi, Y. S. et al. Study on gelatin-containing artificial skin: I. Preparation and characteristics of novel gelatin-alginate sponge. *Biomaterials* **20**, 409–417 (1999).
31. Renvoise, J., Burlot, D., Marin, G. & Derail, C. Adherence performances of pressure sensitive adhesives on a model viscoelastic synthetic film: a tool for the understanding of adhesion on the human skin. *Int. J. Pharm.* **368**, 83–88 (2009).
32. Dąbrowska, A. et al. A water-responsive, gelatine-based human skin model. *Tribol. Int.* **113**, 316–322 (2017).